Check for updates

ADVANCED ELECTRONIC MATERIALS
Open Access
www.advelectronicmat.de

Oxynitride Amorphous Carbon Layer for Electrically and Thermally Robust Bipolar Resistive Switching

*SunHwa Min, Da Seul Hyeon, Gabriel Jang, Jisoo Choi, Jeongwoo Seo, Soyeong Kwon, Dong-Wook Kim, and Jin Pyo Hong**

Advanced resistive random-access memory (ReRAM) devices based on resistive switching (RS) have been intensely studied for future high-density nonvolatile memory devices owing to their high scalability, simplified integration, fast operation, and ultralow power consumption. Among the recently considered active media, diverse carbon-based media have emerged because of numerous benefits of simple chemical composition, desirable speed, and cost-effective scalability. However, these media are still susceptible to undesirable reliability issues, including poor endurance and retention and uncontrollable operation voltage distribution. In this study, an oxynitride amorphous carbon active medium governed by appropriate nitrogen content during growth is introduced to facilitate high electrical stability, such as a distinct pulse endurance of more than 10^7 cycles, a high retention time of 10^5 s at 85 °C, and increased uniformity in the SET/RESET distribution with thermally robust RS stability even at a high annealing temperature of 400 °C. The findings are possibly the result of adapting an sp^2–sp^3 conversion nature assisted by the presence of pyridinic N or pyrrolic N as a substitution reaction.

1. Introduction

In recent years, resistive random-access memory (ReRAM) devices based on resistive switching (RS) behaviors are becoming increasingly vital to satisfying the demands of key memory markets, facilitating high scalability for 3D integration, fast switching speed, and high-reliability features.[1] The ReRAM devices are expected to have numerous benefits, including efficient compatibility with the modern complex complementary metal–oxide–semiconductor processes, ultralow power operation, and affordable fabrication cost with a geometrically simple metal–insulator–metal configuration.[2] Among the active materials developed as storage media in ReRAM devices, carbon-based materials have recently emerged due to their low cost, simple chemical composition, and fast operation speed.[3] Several studies have examined the RS mechanism in these media and offer significant opportunities to improve device performance.[4]

To date, the most recently reported promising active medium has been an oxygenated amorphous carbon (α-CO_x) active layer based on the conversion between the sp^2 conductive filaments (CFs) and sp^3 insulating characteristics caused by bias-dependent oxygen ion drifts.[5] C–C sp^2 bonds are highly conductive due to their graphitic frame while C–C sp^3 bonds are poorly conductive due to their diamond configuration.[6] The corresponding results give rise to two different conduction levels, leading to two representative RS behaviors from sp^2–sp^3 conversion via bias. These α-CO_x layer-based ReRAM devices addressed the increased electrical performance, including the high on/off ratio and appreciable switching speed. However, the widespread utilization of these devices has been hindered by the requirement of high forming voltages and poor stability features.

Furthermore, these devices are highly susceptible to undesirable instability in forming voltages during repeated sweeps, caused primarily by the random rupture/formation events of sp^2 CFs initially generated by the forming process.[7] A compositional change in α-CO_x during thermal annealing also causes the carbon–oxygen bonds to be rearranged as a C–C sp^2 bond, experiencing rapid thermal degradation.[7a] This phenomenon is similar to that frequently observed from the oxide-based active media, in which the oxygen ions are randomly released under

S. H. Min, J. P. Hong
Research Institute for Convergence of Basic Science
Division of Nano-Scale Semiconductor Engineering
Hanyang University
Seoul 04763, South Korea
E-mail: jphong@hanyang.ac.kr

D. S. Hyeon, G. Jang, J. Choi, J. Seo, J. P. Hong
Research Institute of Natural Science
Department of Physics
Hanyang University
Seoul 04763, South Korea

S. Kwon
Department of Physics and New and Renewable Energy Research Center
Ewha Womans University
Seoul 03760, South Korea

D.-W. Kim
Department of Physics
Ewha Womans University
Seoul 03760, South Korea

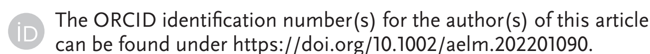
The ORCID identification number(s) for the author(s) of this article can be found under https://doi.org/10.1002/aelm.202201090.

© 2023 The Authors. Advanced Electronic Materials published by Wiley-VCH GmbH. This is an open access article under the terms of the Creative Commons Attribution License, which permits use, distribution and reproduction in any medium, provided the original work is properly cited.

DOI: 10.1002/aelm.202201090

2199160x, 0, Downloaded from https://onlinelibrary.wiley.com/doi/10.1002/aelm.202201090 by Hanyang University Library, Wiley Online Library on [12/02/2023]. See the Terms and Conditions (https://onlinelibrary.wiley.com/terms-and-conditions) on Wiley Online Library for rules of use; OA articles are governed by the applicable Creative Commons License

thermal annealing.[8] Therefore, manipulating electrical and thermal stability under bias is a challenge due to the demands of high-performance practical applications.

To overcome these limitations of α-CO_x layer-based ReRAM devices, our previous study manipulated sp^2-sp^3 bonding ratios by placing a suitable thin Cu layer into the α-CO_x active layer, in which additional Cu—O bonds impacted the proportion of sp^2 bonds and decreased sp^3 bonds in a specific region.[9] The corresponding observations resulted from establishing thick CFs, contributing to the relative increase in device stability. However, practical questions remain concerning poor reliability issues, including endurance/retention features and how the main RS operates or is maintained after higher thermal annealing—a high annealing temperature is required at the back end of the line for practical devices.

Herein, we report the advancing RS characteristics of as-grown and annealed oxynitride amorphous carbon (α-CO_xN_y)-based ReRAM devices by incorporating appropriate nitrogen content into the α-CO_x active layer during growth. The corresponding results exhibit prominent RS reliability features, including high pulse endurance (>10^7 cycles), sufficient retention time at 85 °C (>10^5 s), and extremely narrow switching distribution. We verify the functionality of the additional nitrogen on the improved electrical and thermal performance, which may be governed by the presence of the C–N bond comprising pyridinic N or pyrrolic N as a substitution reaction, using intensive structural observations.

2. Results and Discussion

Two samples are chosen as follows: typical Pt/α-CO_x/W (Sample A) and new Pt/α-CO_xN_y/W (Sample B) stacks for comparison of electrical and thermal RS characteristics. **Figure 1**a illustrates the representative schematics of Samples A and B, in which the cross-sectional TEM image of Sample B enlarged by a red dotted rectangle indicates the uniformly grown 12 nm-thick oxynitride amorphous carbon active layer (α-CO_xN_y) between the Pt (inert metal) top and W (active metal) bottom electrodes. The size of each sample is determined by an initially patterned W bottom nano-plug-shaped contact pad. During the device operation, a Pt top electrode is biased by being grounded to the W electrode under a typical compliance current of 10 mA, preventing the permanent breakdown of each sample. Both samples require typical electroforming for the RS activation under a negative voltage to the Pt top electrode. Both samples also required a typical electroforming process for the RS activation under a negative voltage to the Pt top electrode, as seen in Figure S1, Supporting Information. More detailed/similar *I–V* responses of Samples A and B under a compliance current of 1 mA are depicted in Figure S2, Supporting Information.

Figure 1b,c illustrates the DC resistance switching (RS) features for Samples A and B at room temperature, in which the DC cycle-to-cycle RS is tested in the sequence of 0 V → 1.7 V → 0 V → −3 V → 0 V. The HRS of Sample A provides the random distribution in the range from several 10^3 to 10^5 Ω at a reading voltage of 0.1 V only during the 100 consecutive cycles, while the HRS of Sample B remains mostly unaffected even over the 1000 DC cycles. Such an increase in DC stability of Sample B may be understood based on a possible reduction in random rupture/formation of CF when appropriate nitrogen to the α-CO_x active layer is introduced during growth (a more detailed description is presented later). Figure 1d exhibits the cycle-to-cycle distribution characteristics of Samples A and B. Sample A provides a high fluctuation in HRS states and a slight fluctuation in LRS states. In contrast, Sample B remains mostly unchanged in LRS and slightly varies in HRS. Furthermore, Sample B maintains the 10^2 memory window over repeated 1000 cycles.

Initially, various nitrogen partial pressure-dependent *I–V* features of Sample B are recorded to select an appropriate nitrogen content and ensure augmented *I–V* responses (Figure S3, Supporting Information). The use of 3.2% nitrogen partial pressure results in a higher current on/off ratio and noticeably narrower distribution in a cell-to-cell test than those of different partial pressures during 100 consecutive switching cycles. However, a nitrogen partial pressure of more than 3.2% causes undesirable *I–V* fluctuations. These findings are likely associated with a nitrogen partial pressure-dependent reduction in C–C sp^2 bond contents, as described later. Therefore, appropriate nitrogen incorporation during growth strongly impacts device performance.

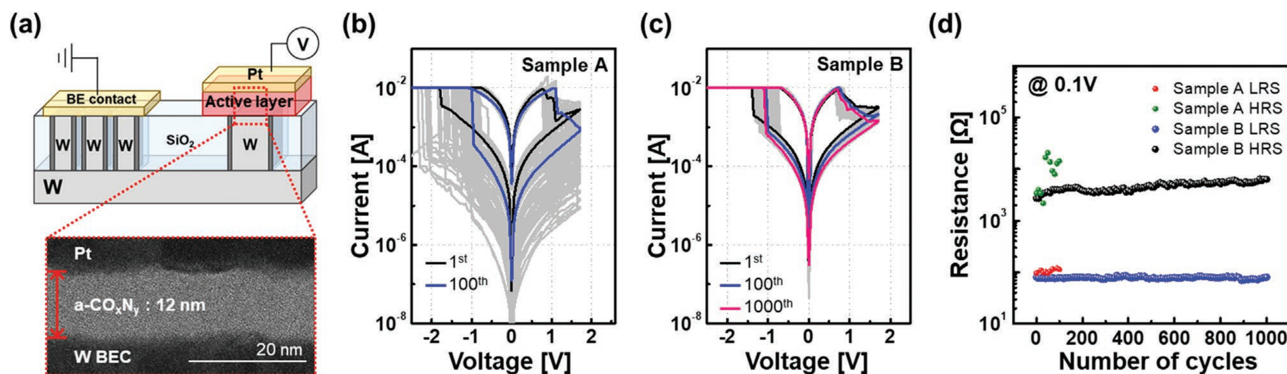

Figure 1. Structural configuration and bipolar RS response. a) Representative schematic of Samples A and B and cross-sectional TEM image of Sample B. b,c) DC endurance tests of Sample A (b) and Sample B (c) for the first cycle (black), 100 consecutive cycles (blue), and 1000 consecutive cycles (pink). d) DC endurance characteristics for the LRS and HRS of Samples A and B, in which Sample B reveals highly stable RS features up to 1000 DC consecutive measurements compared with those of Sample A.

© 2023 The Authors. Advanced Electronic Materials published by Wiley-VCH GmbH

2199160x, 0, Downloaded from https://onlinelibrary.wiley.com/doi/10.1002/aelm.202201090 by Hanyang University Library, Wiley Online Library on [12/02/2023]. See the Terms and Conditions (https://onlinelibrary.wiley.com/terms-and-conditions) on Wiley Online Library for rules of use; OA articles are governed by the applicable Creative Commons License

In this study, Sample B is prepared at a nitrogen partial pressure of 3.2%. Furthermore, a device-size dependent analysis is conducted to identify the possible conduction nature of RS behaviors by adopting initially patterned W bottom electrodes in the range of 1.4 µm to 81 nm (Figure S3, Supporting Information), in which the device size is determined by the bottom electrode size.

The electroforming voltages of all samples remain approximately constant at −2.3 V (± 0.2 V), regardless of device size. This observation reflects the CF-type nature consistent with previous studies.[10] As indirect evidence of the underlying mechanism observed from the above analyses, the active layer thickness-dependent forming voltages of Samples A and B are also monitored (Figure S5, Supporting Information). The electroforming voltage increases with increasing active layer thickness, likely caused by the CF-type behavior in Samples A and B. To test the electrical stability of Sample B, we have chosen the 12 nm thick Sample B because it provided the best uniform operating voltage, cell-to-cell distribution, and endurance, even though a slight increase in the forming voltage was observed, as seen in Figure S6, Supporting Information.

In validating the cycle-to-cycle stability and reproducibility features as crucial parameters in practical ReRAM applications, the cumulative probability distributions of SET and RESET voltages for Samples A and B are monitored at a reading voltage of +0.1 V during the first 100 consecutive sweeps. **Figure 2**a plots the cumulative probability distributions of LRS (black) and HRS (red) for Samples A and B, where the current on/off ratios for Samples A and B are 1.2×10^1 and 10^2, respectively. Figure 2b exhibits the statistical distribution of the SET and RESET voltages for Samples A (upper) and B (lower) over the consecutive 100 DC sweeps. Sample B reveals a distinct narrower variation in V_{reset} (−1.4 to −0.95 V) and V_{set} (0.7 to 0.8 V) than those of Sample A. The SET and RESET voltage distributions of Sample A are in the range from −2.35 to −0.6 V and 0.8 to 1.15 V, respectively while Sample B ensures high cycle-to-cycle uniformity in its RS characteristics.

Typical ReRAM devices frequently exhibit a wide range of distribution behaviors in operating voltage and resistance states—strongly expressed by the random rupture/formation models of CFs mainly induced from the random oxygen ion movement and diffusion events under electrical pulses.[11] However, introducing the appropriate amount of nitrogen partial pressure in this study contributes to a distinct increase in the LRS and HRS stability of Sample B. More cell-to-cell distribution results of Samples A and B are given in Figure S7, Supporting Information. Figure 2c plots the retention features of Samples A and B collected at 85 °C and a read bias of 0.1 V. The corresponding observations illustrate a slight variation in Sample B's currents without significant degradation over 10^5 s. In contrast, Sample A experiences a sudden conductance drop in LRS and HRS only after 3×10^3 s and 4×10^3 s, respectively. These results validate the highly stable retention of Sample B. The consecutively applied voltages might represent the presence of the randomly ruptured/generated CFs, causing the unintendedly weakened connection strength of CFs.[12]

Figure 2d plots the pulse endurance responses of Samples A (upper) and B (lower), in which the measurements are conducted with consecutive AC voltage pulses to verify the electrical stability under $V_{set} = -1.7$ V and $V_{reset} = +2.2$ V, as seen in Figure S8, Supporting Information. The writing pulse widths and reading voltages are 1 µs and 0.2 V, respectively. Sample B identifies an increase in reliable characteristics over 10^7 cycles, while Sample A provides the randomly distributed resistances in HRS and LRS, possibly caused by the randomly distributed oxygen ions in α-CO_x active layer containing diverse electrophilic sp^2 bond sites.

The pulse responses for forming, SET, and RESET states are tested to validate the pulse endurance of Samples A and B (Figures S9 and S10, Supporting Information). In this analysis, the chosen voltages are several times larger than those taken

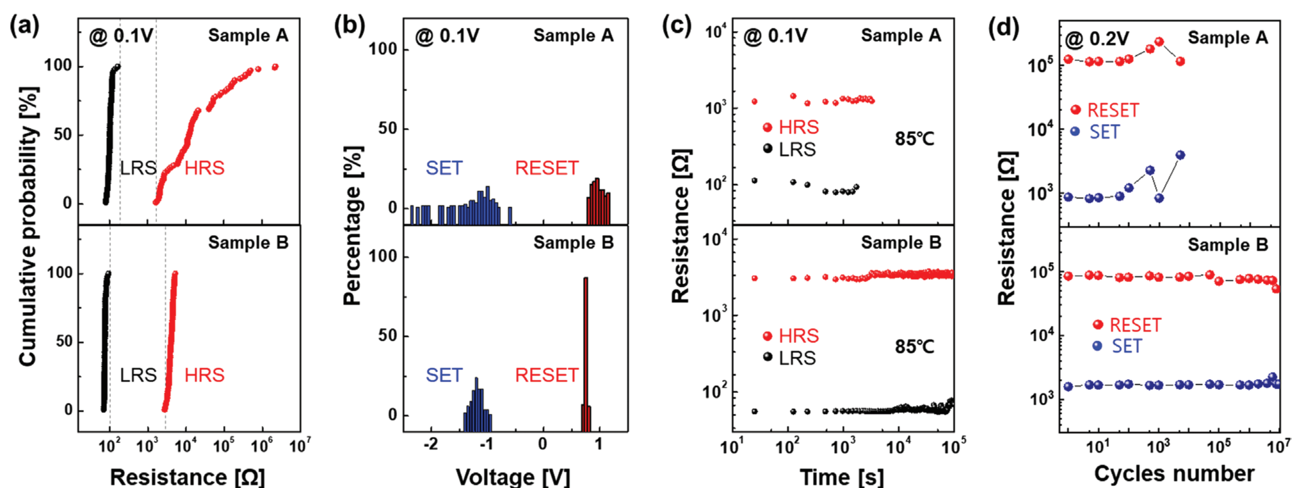

Figure 2. DC and pulse reliability analyses. a) Cumulative resistance probability at the LRS (black) and HRS (red), and b) statistical distributions of SET (blue) and RESET (red) voltages for Samples A (upper) and B (lower) for the first 100 DC sweep cycles. Sample B exhibits a significantly narrower variation than that of Sample A. c) Retention characteristics of the LRS and HRS for Samples A and B, in which the measurements are performed at 85 °C with a read bias of 0.1 V. Sample B leads to sufficiently stable features without significant degradation. d) Pulse endurance performance of Samples A and B, in which Sample B proves more reliable characteristics over 10^7 cycles.

© 2023 The Authors. Advanced Electronic Materials published by Wiley-VCH GmbH

2199160x, 0, Downloaded from https://onlinelibrary.wiley.com/doi/10.1002/aelm.202201090 by Hanyang University Library, Wiley Online Library on [12/02/2023]. See the Terms and Conditions (https://onlinelibrary.wiley.com/terms-and-conditions) on Wiley Online Library for rules of use; OA articles are governed by the applicable Creative Commons License

for the DC RS measurement since the relatively shorter pulse width is used in the pulse analyses than that of the DC measurement approach. Figure S9a–c, Supporting Information shows the forming, SET, and RESET voltages of Sample B, which are −3.4, −1.6, and 2.4 V, respectively. Figure S10a–c, Supporting Information exhibit the forming, SET, and RESET voltages of Sample A, which are −2.4, −1.42, and 1.4 V, respectively. The switching speed is determined by employing the square wave input signals to examine the memory characteristics of Samples A and B. Figure S9d,e, Supporting Information displays the SET and RESET pulses applied to Sample B with −4.5 V for 1 µs and 3.2 V for 2 µs, respectively. The corresponding results confirmed the switching speeds (SET < 55 ns at −2.25 V and RESET < 50 ns at 2.8 V) for Sample B. Figure S10d,e, Supporting Information exhibit the switching speeds of Sample A, where the SET pulse (−4 V, 1 µs) is used to switch the Sample A between LRS and HRS. Subsequently, the RESET pulse (3 V, 2 µs) is applied to Sample A. The corresponding results are 55 ns at −2.9 V and 50 ns at 2.6 V, respectively.

XPS depth profile analyses were conducted to clarify the chemical composition and bonding states associated with carbon hybridization bonds in Samples A and B. **Figure 3**a,b illustrate the representative XPS depth profiles for Samples A and B. Both samples reveal the typical C 1s, O 1s, and W 4f elements, except N 1s in Sample B, where the N1s elements are uniformly well-distributed throughout the active layer. Figure 3c,d plot the C1s spectra of Samples A and B, collected over an etching time of 100 s. The C1s core-level spectra for Samples A and B are determined by the sp^2 (284.3 ± 0.1 eV), sp^3 (285.2 ± 0.1 eV), and C_{sp2}–N (285.8 eV), where the C–O group directly relates to C–O (286.4 eV), C=O (288 eV), and COOH (289.4 eV).[13] Figure 3d exhibits the clear presence of a C–N bond in Sample B. Previous studies on the α-CO_x-based ReRAMs have demonstrated that the sp^2 bonds constituting the CF paths reflect metallic properties, while the C–C sp^3 bonds incorporated with O ions represent insulating characteristics. This implies that the presence of a proper amount of C–C sp^2 bonds is highly related to the RS nature.[9,14]

Figure 3e plots the N 1s binding energy of Sample B, which can be de-convoluted into three peaks. Each peak corresponds to the pyridinic N, pyrrolic N, and oxidized N at 398.5, 400.1, and 403 eV, respectively.[15] The two dominant peaks at 398.5 and 400.1 eV reflect the C–N sp^3 and C–N sp^2 bonds, respectively.[16] As described by previous studies,[17] the pyridinic N bonds with two carbon atoms at the boundary or defect of amorphous carbon bonding states, has a lone pair of electrons, and donates one p electron to the π system. Furthermore, the N atom in pyrrolic N substitutes a carbon atom of the five-membered ring and gives two p electrons to the π system. Consequently, the N atoms integrated with the two dominant bonds serve as substitutional doping elements at carbon sites. A more detailed role of p electrons generated by substitutional bonds will be described later. However, in this work, we excluded the possibility of the RS effect arising from the possible WO_x formation that may be formed during oxygen plasma sputtering due to the following reasons: Figure S11a,b, Supporting Information plot the O 1s spectra for Samples A and B collected at an etching time of 280 s on the active layer/W interfaces. The corresponding observations suggest that the oxygen atoms are mainly bound to carbon atoms without exhibiting the formation of the WO_x layer at the active layer/W interfaces.

Figure S12, Supporting Information reveals that an increase in nitrogen partial pressures contributes to an increase in the C–N/C–C sp^3 bond amount in C 1s and a decrease in the C–C sp^2 area. It is plausible that during the α-CO_xN_y deposition process, N interfered with the binding of oxygen by substitutional binding to the C site. Introducing a large amount of nitrogen (for example, nitrogen partial pressure of 12.5%) produces numerous C–N bonds in the active layer, possibly reflecting the difficulty in sp^2–sp^3 conversion under bias. A

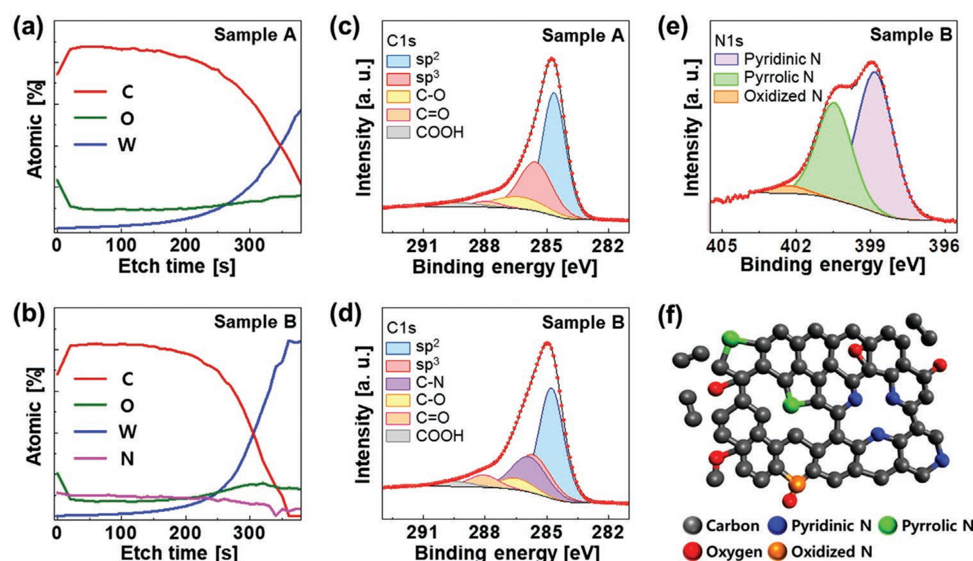

Figure 3. XPS analysis and possible chemical structural model. a,b) XPS depth profiles of Sample A (a) and Sample B (b) for C, O, W, and N elements. c,d) XPS spectra of the C 1s region of Sample A (c) and Sample B (d), where Sample B reveals the presence of the C–N bond peak. e) XPS spectra of N 1s for Sample B with three dominant peaks of pyridinic, pyrrolic, and oxidized N, where the pyridinic N seems to be the predominant component. f) Potential chemical bonding schematics of Sample B, including the possible three deconvoluted nitrogen configurations.

© 2023 The Authors. Advanced Electronic Materials published by Wiley-VCH GmbH

2199160x, 0, Downloaded from https://onlinelibrary.wiley.com/doi/10.1002/aelm.202201090 by Hanyang University Library, Wiley Online Library on [12/02/2023]. See the Terms and Conditions (https://onlinelibrary.wiley.com/terms-and-conditions) on Wiley Online Library for rules of use; OA articles are governed by the applicable Creative Commons License

2199160x, 0, Downloaded from https://onlinelibrary.wiley.com/doi/10.1002/aelm.202201090 by Hanyang University Library, Wiley Online Library on [12/02/2023]. See the Terms and Conditions (https://onlinelibrary.wiley.com/terms-and-conditions) on Wiley Online Library for rules of use; OA articles are governed by the applicable Creative Commons License

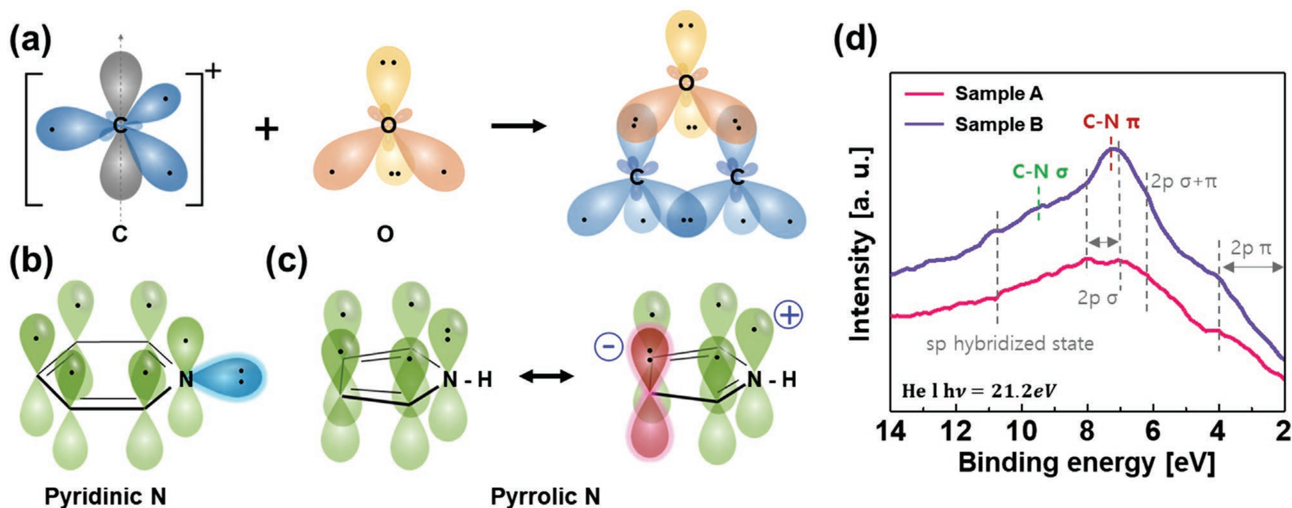

Figure 4. Hybrid orbital geometries and UPS analyses. a) Schematic illustration of bonds between an electrophilic sp^2 hybridized orbital of carbon and oxygen atomic orbital, where the end-to-end overlap between the atomic orbitals indicates the presence of sp^3 hybrid orbitals in the C atom. b) Representation of the sp^2 hybrid orbital bonding between an electrophilic carbon and pyridinic N. The unshared electron pair of pyridinic N is in an sp^2 orbital parallel to the six-carbon membered ring. c) Orbital structure of pyrrolic N incorporated in the five-membered heterocyclic ring and pyrrolic N resonance structure. Pyrrole's every atom of the five-membered ring is nucleophilic by resonance. d) UPS spectra of Sample A (pink) and Sample B (purple) measured with He I (21.2 eV) radiation, confirming the presence of the C–N π peak and σ peak in Sample B.

closer investigation of the N 1s spectra at each partial pressure also implies that an increase in nitrogen partial pressures represents a decrease in the pyridinic N component and an increase in the pyrrolic N component. Therefore, a choice of the appropriate amount of nitrogen has a significant impact on the occurrence of electrically and thermally stable sp^2–sp^3 conversion in this study. Thus, in line with the above XPS observations, a possible schematic of nitrogen incorporation in the α-CO_x layer is illustrated in Figure 3f, with the possible N locations in α-CO_xN_y layer.

The orbitals in each active layer are also considered to possibly predict the possible chemical bond states of Samples A and B. **Figure 4**a illustrates a possible schematic for bonds between the sp^2 hybridized orbital of the C atom and the sp^3 orbital of the O atom. The sp^2 hybridized orbital of the C atom would have positive charges functioning as electrophilic sites (Lewis acids), attractively interacting with electron-rich sites. As illustrated in Figure 4b, the pyridinic N generates the C–N σ bond parallel to the six-carbon membered ring and has an unshared electron pair in the same plane. Therefore, the C–N bonds associated with the pyridinic N are likely related to the reduction in sp^2 orbits of C atoms.

Figure 4c exhibits the representative orbital (left) and resonance (right) structures for the pyrrolic N incorporated with the C ring, in which each C atom in the pyrrolic N generates the negative formal charge by the C–N π bond.[53] Thus, a negative charge characteristic of the C–N bond may represent a reduction in the C–O bonds. However, this scenario may suggest that the C–C sp^2 bond can be stabilized by the N as a substitution bond when appropriate nitrogen is introduced. The UPS (He I) valence band spectra are recorded to gain further insight into the electronic states of the α-CO_xN_y layer (Figure 4d). The spectra of Samples A and B identify the presence of six component peaks in the valence band structure in the range of 2 to 14 eV. Both samples provided four similar peaks, assigned as C–C 2p π at ≈4 eV, C–C 2p π–σ overlap at 6.2 eV, C–C 2p σ at 7–8 eV, and 2s–2p mixed states at 10.5 eV. However, Sample B provides two additional peaks of the C–N 2p π and C–N 2p σ electronic states at 7.2 eV and at 9 eV, respectively.[18] These two peaks may suggest the probability of reducing the bonds between the C–C sp^2 and O ions caused by the unshared electron pair of pyridinic N and the negative formal charge of pyrrolic N, as described previously.

Based on the above observations, the possible RS nature for Samples A and B is proposed in **Figure 5**. The starting concept is as follows: in both samples, the C–C sp^2 bonds constituting the CF paths convert to the C–C sp^3 bonds through the possible reaction between the sp^2 bonds and O induced by bias-dependent oxygen ion drift events. In addition, C–C sp^3 bonds directly relate to the rupture of CF paths. In contrast, a reverse bias enables the C–C sp^3 bonds to be converted to the C–C sp^2 bonds by eliminating oxygen ions. As described in previous our work, the formation of CF came from the increase in C–C sp^2 bonds in the active layer. The rupture of CF is highly related to an increase in C–C sp^3 ratio, thereby providing a lower C–C sp^2 intensity in the active layer.[7c] Figure 5a displays the pristine state of the as-grown α-CO_x layer containing randomly dispersed oxygen ions over the entire carbon oxide layer. A negative bias on the Pt top electrode drives oxygen ions to flow toward the W bottom electrode as an electroforming step, generating the local CFs by forming sp^2 bonds (Figure 5b). Under a positive bias, the initially created CFs (possibly filament 1 in Sample A) are annihilated as a RESET step by the oxygen ions drifting to the TE (Figure 5c). However, the SET step of Sample A may generate the random creation of other CF paths (filament *n*) at different locations.

Thus, the corresponding results are highly relevant to the unstable RS behaviors of Sample A under repeated sweeps (Figure 5d): Sample A would experience the indiscriminately distributed oxygen ions, creating the random rupture/formation

 © 2023 The Authors. Advanced Electronic Materials published by Wiley-VCH GmbH

2199160x, 0, Downloaded from https://onlinelibrary.wiley.com/doi/10.1002/aelm.202201090 by Hanyang University Library, Wiley Online Library on [12/02/2023]. See the Terms and Conditions (https://onlinelibrary.wiley.com/terms-and-conditions) on Wiley Online Library for rules of use; OA articles are governed by the applicable Creative Commons License

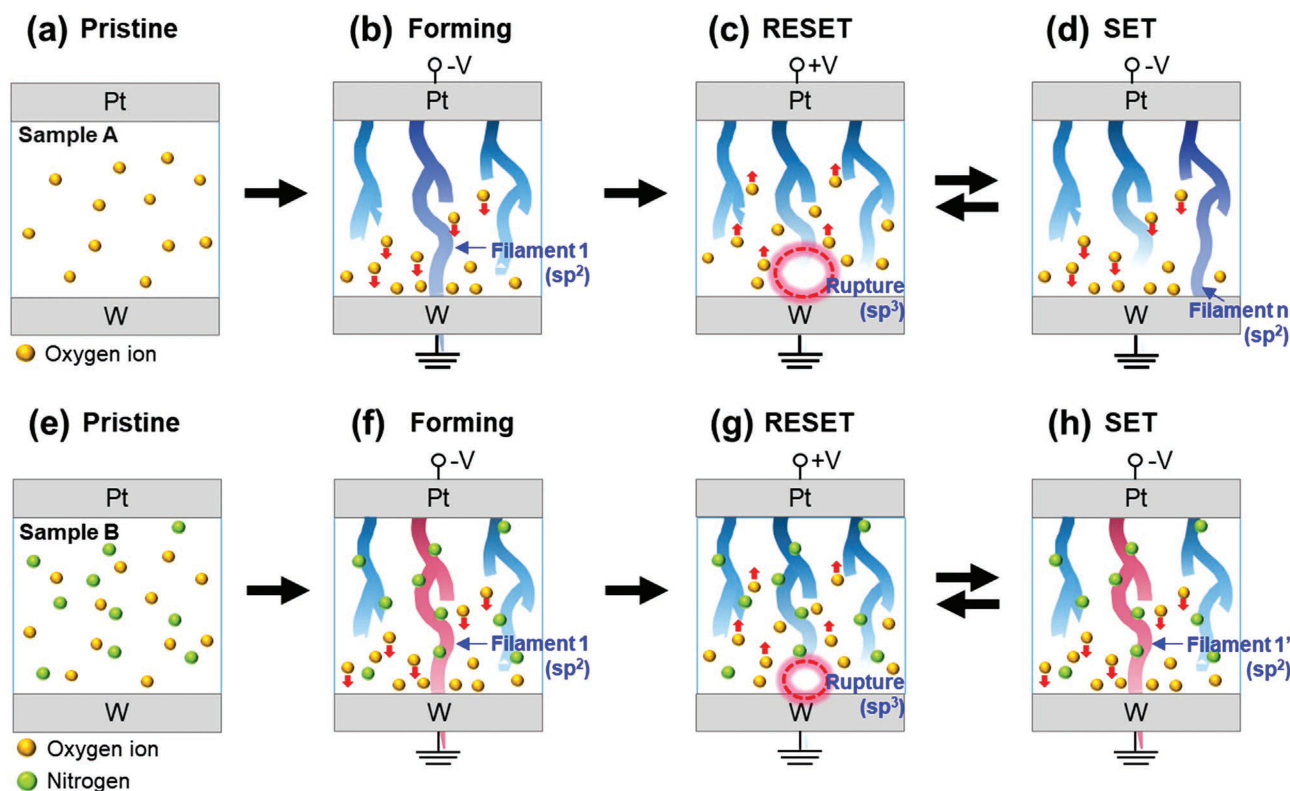

Figure 5. Proposed RS nature for Samples A and B. a–d) Schematic illustration of RS process based on bias-dependent oxygen ion drift in Sample A. a) Pristine state containing randomly dispersed oxygen ions in an entire carbon oxide layer. b) Electroforming step creating the local CFs of sp^2 bonds by the movement of oxygen ions toward the BE under a negative bias on the TE. c) RESET step causing the annihilation of the initial CF path (possibly filament 1) by the reverse movement of oxygen ions to the TE under a positive bias. d) SET step providing random creation of other CF paths (filament *n*) at different locations. Consequently, the corresponding results lead to unstable switching behaviors of Sample A. e–h) Schematic of RS process in Sample B. e) Pristine state containing randomly distributed oxygen ions and additional nitrogen atoms in an entire α-CO_xN_y layer. f) Electroforming step generating the local CFs of sp^2 bonds by the movement of only oxygen ions towards the BE under a negative bias on the TE, where the nitrogen atoms remain unaffected via bias. g) RESET step leading to a partial rupture of the CF path (filament 1) pre-existing from the electroforming process. h) SET step generating the main CFs (filament 1) governed by the electroforming step caused by the pre-existing nitrogen atoms related to the sp^2 orbital. Thus, suitable integration of nitrogen in Sample B increases the electrical stability.

of the sp^2 bonds during consecutive sweeps. In the Sample B case, Figure 5e exhibits the possible pristine state of Sample B, including the randomly distributed oxygen ions and additional nitrogen atoms in an entire α-CO_xN_y layer. The nitrogen components are mostly pyridinic N and pyrrolic N because of the substitution reaction with the sp^2 bonds. The electroforming step generates the local CFs of C–C sp^2 bonds by the movement of only oxygen ions toward the BE under a negative bias on the TE (Figure 5f). The N atoms remain mostly unaffected via bias, as seen in Figure S13, Supporting Information, in which the typical bipolar RS behavior was not clearly observed from the pure α-CN_x-based device with no oxygen element. But it can be expected that the nitrogen atom would also have a slight impact on the RS behavior. The RESET step under a positive bias causes oxygen ions to move toward the CFs or TE, rupturing the initial CFs (possibly filament 1 in Sample B) created by the electroforming step (Figure 5g). However, in a SET step of Sample B, the proper presence of pyridinic N and pyrrolic N as substitution reactions with sp^2 bonds permits the initial CFs (filament 1′) created by the electroforming step possibly to be restored (Figure 5h) even though the CFs will not be entirely linked with the RS: the rupture/formation of the CFs initially determined by the electroforming step is likely to be a critical factor in enabling the achievement of the stable RS behaviors in Sample B. However, more research is required to clarify the deterministic mechanism for electrically robust RS features observed when appropriate nitrogen is introduced.

It is well-known that the conduction nature of the RS device can be understood on a log–log scale. To do this, the *I*–*V* responses in Figure 1b,c are redrawn in a double log scale, as shown in Figure S14, Supporting Information. The LRSs of Samples A and B in the whole bias region are close to almost one, implying Ohmic conduction nature.[19] On the other hand, the HRSs of both samples exhibit two different slope regions in low and high voltage ranges, respectively. Therefore, both samples exhibited the slope of one in a low-voltage region and a nonlinear increase in a high-voltage region. The latter likely links to the trap-related space charge limited conduction (SCLC) nature.[20] The representative log-log *I*–*V* curves of Samples A and B are given in Figure S14, Supporting Information.

Post-annealing is a generic approach for validating thermal stability issues due to the demand for a high temperature at the

 © 2023 The Authors. Advanced Electronic Materials published by Wiley-VCH GmbH

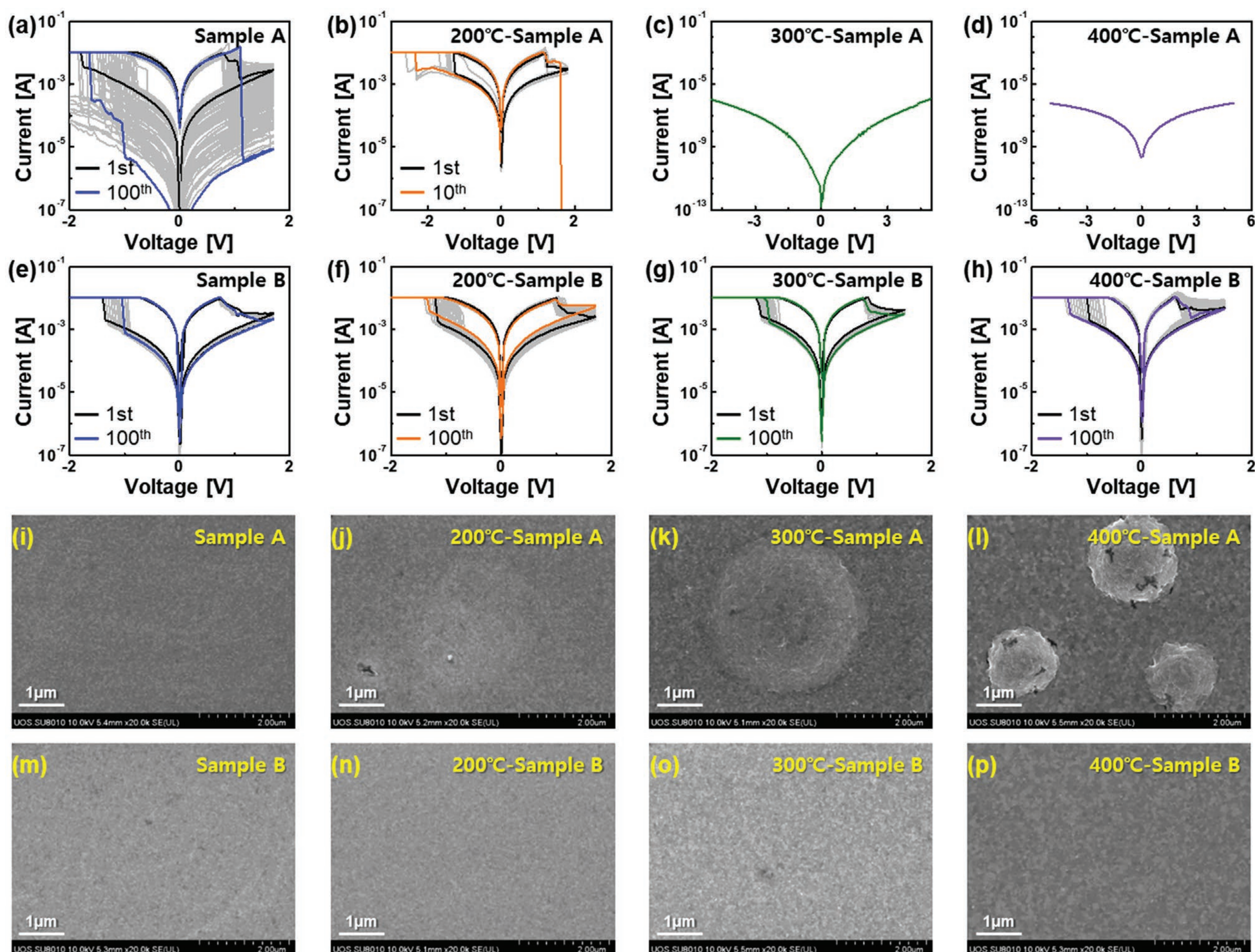

Figure 6. Thermal stability test and SEM images for Samples A and B under annealing. a–h) Representative *I–V* responses of Samples A and B for the 100 consecutive DC cycles at various annealing temperatures: a–d) as-grown, 200, 300, and 400 °C-annealed Sample A; e–h) as-grown, 200, 300, and 400 °C-annealed Sample B. After exceeding 200 °C, Sample A exhibits rapid electrical degradation in RS, while Sample B provides a thermally promising feature of Sample B even at an annealing temperature of 400 °C. i–p) SEM images of Samples A and B at various annealing temperatures: i–l) as-grown, 200, 300, and 400 °C-annealed Sample A; m–p) as-grown, 200, 300, and 400 °C-annealed Sample B.

back end of the line at approximately 400 °C.[21] Therefore, both samples are carefully annealed at 200, 300, and 400 °C for 1 h in an argon (Ar) atmosphere. **Figure 6**a–d plot the annealing-dependent *I–V* characteristics of Sample B. The as-grown state of Sample B exhibits relatively stable RS behaviors up to 100 consecutive sweeps. However, Sample A experiences a rapid thermal degradation only after annealing at 200 °C, and then Sample A remains in an insulating state: no conduction paths in Sample A are generated after annealing at temperatures greater than 300 °C. The corresponding results are likely linked with the distinct suppression or loss of oxygen ions, which significantly affects the rupture/formation of CFs—a previous study predicted an abrupt oxygen vaporization event in oxide materials via a higher annealing process.[22]

Surprisingly, Sample B ensures the thermally robust annealing *I–V* characteristics without any degradation: continuous DC *I–V* features of Sample B are maintained even at a higher annealing temperature of 400 °C, as illustrated in Figure 6e–h, in which the on/off ratio is slightly decreased with increasing annealing temperatures. Thus, SEM measurements on both samples are conducted to provide indirect evidence for the above annealing observations. As illustrated in Figure 6i–p, the top electrode surface morphologies of Sample A are significantly affected by post-annealing, while Sample B maintains the initially grown top electrode surface, regardless of the annealing temperature. Typically, a dramatic variation in surface states of Sample A occurs from 200 °C, followed by large surface deformations. After post-annealing at 400 °C, a black image seems to be likely a carbon material without oxygen elements.

The XPS depth profiles for both samples are monitored after annealing at 400 °C to clarify the possible contribution to the thermally robust electrical features in annealed Sample B. **Figure 7** exhibits the composition ratios of Pt, C, O, and N elements in the as-grown state of Samples A and B before/after annealing at 400 °C, where each constituent element is collected through Ar etching for 100 s. Figure 7a exhibits the uniformly deposited 12 nm thick active layer of Sample A, as expected. After annealing at 400 °C (Figure 7b), the Pt 4f peak

 © 2023 The Authors. Advanced Electronic Materials published by Wiley-VCH GmbH

2199160x, 0, Downloaded from https://onlinelibrary.wiley.com/doi/10.1002/aelm.202201090 by Hanyang University Library, Wiley Online Library on [12/02/2023]. See the Terms and Conditions (https://onlinelibrary.wiley.com/terms-and-conditions) on Wiley Online Library for rules of use; OA articles are governed by the applicable Creative Commons License

2199160x, 0, Downloaded from https://onlinelibrary.wiley.com/doi/10.1002/aelm.202201090 by Hanyang University Library, Wiley Online Library on [12/02/2023]. See the Terms and Conditions (https://onlinelibrary.wiley.com/terms-and-conditions) on Wiley Online Library for rules of use; OA articles are governed by the applicable Creative Commons License

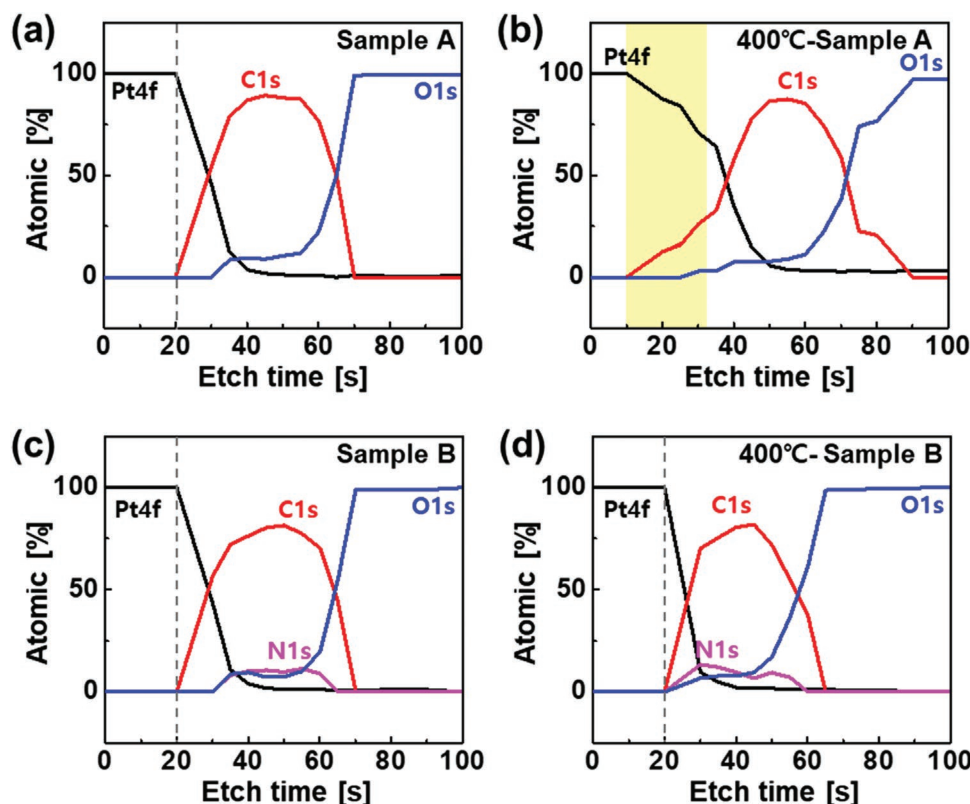

Figure 7. XPS depth profile analyses for Samples A and B as-grown and annealed at 400 °C. a–d) XPS depth profiles of as-grown (a) and 400 °C-annealed (b) Sample A and for as-grown (c) and 400 °C-annealed (d) Sample B for Pt, C, O, and N elements. Sample A provides the presence of the C1s elements in the Pt layer after annealing, whereas, in Sample B, the C1s elements increase until Pt elements decrease even after annealing.

decreases and the C 1s peak increases but partial oxygen ions existing in the active layer out-diffuses to the Pt top electrode via a possible vaporization process, supporting a possible reduction/suppression in oxygen ions initially bonded to the carbon atoms after annealing.

Figure 7c illustrates the uniformly distributed nitrogen and oxygen ions over the entire area of the active layer in the as-grown state of Sample B. After annealing at 400 °C (Figure 7d), the peaks of the Pt 4f and C 1s reveal a similar tendency to those of as-grown states, implying that Sample B seems to be primarily unaffected by a thermal breakdown event frequently observed from previously reported α-CO_x-based devices when appropriate nitrogen is introduced during growth. The peaks of O 1s and N 1s seem to shift slightly toward the Pt layer without dramatic variation.

Previous studies suggested that the oxidized compounds can be vaporized and expanded under annealing.[8] However, using an appropriate amount of nitrogen with oxygen may provide an inherently low thermal expansion rate of the C–N during oxygen vaporization compared with those prepared by pure oxygen gas.[23] Accordingly, because the C–C sp^2 and oxygen in Sample A are sterically bonded in a 3D structure, an empty space appears in the active layer. However, the nitrogen as substitution reaction with a C–C sp^2 bond or ring likely enables the appearance of weak van der Waals force between carbon atoms, allowing for a reduction in the 3D space: Sample B containing appropriate nitrogen may have relatively less agglomerated space.

3. Conclusion

We address the electrical and thermal increase in RS performance by the introduction of appropriate nitrogen on Pt/α-CO_x/W devices during growth. The extensive analyses of the structural and electrical observations imply that the presence of nitrogen component possibly reduces random rupture/formation of directly related sp^2 CFs bonded by the pyridinic/pyrrolic N as a substitution reaction: the less-C–C sp^2 sites bonded by O ions seem to be critical to electrical and thermal stability even after higher annealing of 400 °C. Thus, we anticipate that the appropriate use of nitrogen could be generalized and extended to establish carbon-based RS devices, although additional experiments are necessary to enhance further device performance including memory windows.

4. Experimental Section

Sample Preparation: Samples A and B were prepared on the nano-sized W bottom electrodes, defining the sample size. In this experiment, the conventional on-axis sputtering approach generated oxidation etching by reacting oxygen plasma with carbon ions during the growth, limiting the direct deposition of both active layers. Therefore, an off-axis sputtering approach was specifically selected to minimize active layer etching events during the growth, where the target was perpendicular to the substrate. The α-CO_xN_y was prepared by employing a graphite target via reactive sputtering at the base and working pressure of 1×10^{-7} Torr

 © 2023 The Authors. Advanced Electronic Materials published by Wiley-VCH GmbH

and 3×10^{-3} Torr, respectively. The Ar/O_2 sputtering gas flow was fixed at 20/1 sccm, in which the nitrogen gas was in the range of 0 to 12.5% to achieve the optimum growth conditions for various α-CO_x and α-CO_xN_y active layers. A DC plasma power of 110 W was used to deposit the active layer at room temperature.

Sample Characterization: All the DC and pulse *I–V* electrical features were monitored in the air at room temperature using the Keithley 4200 semiconductor parameter analyzer (Keithley 4200 SPA, Keithley Instrument, Inc.). A field emission scanning electron microscope (FE-SEM), X-ray photoelectron spectroscopy (XPS), and UV photoelectron spectroscopy (UPS) were used to verify the chemical characteristics of both active layers. First, the SEM images were captured with a HITACHI (SU8010) system at an acceleration voltage of 10 keV and a current emission of 10 µA. Second, with the K-Alpha+ measurements, XPS measurements were conducted to identify the possible chemical bonding and component distribution. Finally, UPS analyses were conducted with the 21.2 eV photon irradiation (He I line).

Supporting Information

Supporting Information is available from the Wiley Online Library or from the author.

Acknowledgements

S.M. and D.S.H. contributed equally to this work. This research was supported by the National Research Foundation of Korea (NRF) (NRF-2021M3F3A2A01037750).

Conflict of Interest

The authors declare no conflict of interest.

Data Availability Statement

The data that support the findings of this study are available from the corresponding author upon reasonable request.

Keywords

off-axis reactive sputtering, oxynitride amorphous carbon layer, pyridinic-nitrogen bonds, pyrrolic-nitrogen bonds, sp^2 bond conductive filaments

Received: September 26, 2022
Revised: November 14, 2022
Published online:

[1] a) J. J. Yang, D. B. Strukov, D. R. Stewart, *Nat. Nanotechnol.* **2013**, *8*, 13; b) H. S. P. Wong, H. Y. Lee, S. Yu, Y. S. Chen, Y. Wu, P. S. Chen, B. Lee, F. T. Chen, M. J. Tsai, *Proc. IEEE* **2012**, *100*, 1951; c) F. Zahoor, T. Z. Azni Zulkifli, F. A. Khanday, *Nanoscale Res. Lett.* **2020**, *15*, 90; d) D. Ielmini, *Semicond. Sci. Technol.* **2016**, *31*, 063002.

[2] a) F. Pan, S. Gao, C. Chen, C. Song, F. Zeng, *Mater. Sci. Eng., R* **2014**, *83*, 1; b) S. Slesazeck, T. Mikolajick, *Nanotechnology* **2019**, *30*, 352003; c) J.-M. Hung, C.-X. Xue, H.-Y. Kao, Y.-H. Huang, F.-C. Chang, S.-P. Huang, T.-W. Liu, C.-J. Jhang, C.-I. Su, W.-S. Khwa, *Nat. Electron.* **2021**, *4*, 921; d) B. Govoreanu, G. S. Kar, Y. Y. Chen, V. Paraschiv, S. Kubicek, A. Fantini, I. P. Radu, L. Goux, S. Clima, R. Degraeve, N. Jossart, O. Richard, T. Vandeweyer, K. Seo, P. Hendrickx, G. Pourtois, H. Bender, L. Altimime, D. J. Wouters, J. A. Kittl, M. Jurczak, in *2011 Int. Electron Devices Meeting*, IEEE, Piscataway, NJ, USA **2011**, https://doi.org/10.1109/IEDM.2011.6131652; e) H. Bazzi, A. Harb, H. Aziza, M. Moreau, A. Kassem, *Analog Integr. Circuits Signal Process.* **2021**, *106*, 351; f) E. W. Cowell III, N. Alimardani, C. C. Knutson, J. F. Conley Jr, D. A. Keszler, B. J. Gibbons, J. F. Wager, *Adv. Mater.* **2011**, *23*, 74.

[3] a) A. Sebastian, A. Pauza, C. Rossel, R. M. Shelby, A. F. Rodríguez, H. Pozidis, E. Eleftheriou, *New J. Phys.* **2011**, *13*, 013020; b) Y. Chai, Y. Wu, K. Takei, H.-Y. Chen, S. Yu, P. C. Chan, A. Javey, H.-S. P. Wong, *IEEE Trans. Electron Devices* **2011**, *58*, 3933; c) E. C. Ahn, H.-S. P. Wong, E. Pop, *Nat. Rev. Mater.* **2018**, *3*, 18009; d) T. J. Raeber, Z. C. Zhao, B. J. Murdoch, D. R. McKenzie, D. G. McCulloch, J. G. Partridge, *Carbon* **2018**, *136*, 280.

[4] a) A. Sawa, *Mater. Today* **2008**, *11*, 28; b) M. Lanza, H. S. P. Wong, E. Pop, D. Ielmini, D. Strukov, B. C. Regan, L. Larcher, M. A. Villena, J. J. Yang, L. Goux, *Adv. Electron. Mater.* **2019**, *5*, 1800143; c) J. J. Yang, I. H. Inoue, T. Mikolajick, C. S. Hwang, *MRS Bull.* **2012**, *37*, 131; d) S. Ambrogio, S. Balatti, S. Choi, D. Ielmini, *Adv. Mater.* **2014**, *26*, 3885.

[5] a) G. Khurana, P. Misra, R. S. Katiyar, *J. Appl. Phys.* **2013**, *114*, 124508; b) Y.-J. Chen, K.-C. Chang, T.-C. Chang, H.-L. Chen, T.-F. Young, T.-M. Tsai, R. Zhang, T.-J. Chu, J.-F. Ciou, J.-C. Lou, *IEEE Electron Device Lett.* **2014**, *35*, 1016; c) T. Raeber, A. Barlow, Z. Zhao, D. McKenzie, J. Partridge, D. McCulloch, B. Murdoch, *Nanoscale* **2018**, *10*, 20272; d) P. K. Enaganti, A. Kothuru, S. Goel, *J. Mater. Res.* **2022**, *37*, 3976.

[6] a) J. Robertson, *Mater. Sci. Eng., R* **2002**, *37*, 129; b) C. Pirlot, I. Willems, A. Fonseca, J. B. Nagy, J. Delhalle, *Adv. Eng. Mater.* **2002**, *4*, 109.

[7] a) C. A. Santini, A. Sebastian, C. Marchiori, V. P. Jonnalagadda, L. Dellmann, W. W. Koelmans, M. D. Rossell, C. P. Rossel, E. Eleftheriou, *Nat. Commun.* **2015**, *6*, 8600; b) B. Murdoch, T. Raeber, A. Barlow, D. McCulloch, J. Partridge, *Appl. Phys. Lett.* **2018**, *112*, 242903; c) S. M. Jin, H. J. Kim, D. S. Woo, S. M. Jung, D. E. Kim, T. H. Shim, J. G. Park, *Adv. Electron. Mater.* **2022**, *8*, 2101083.

[8] a) Q. Song, S. Cao, R. H. Pritchard, B. Ghalei, S. A. Al-Muhtaseb, E. M. Terentjev, A. K. Cheetham, E. Sivaniah, *Nat. Commun.* **2014**, *5*, 4813; b) S. Won, S. Y. Lee, J. Park, H. J. S. R. Seo, *Sci. Rep.* **2017**, *7*, 10186; c) C. Yao, M. Ismail, A. Hao, S. K. Thatikonda, W. Huang, N. Qin, D. Bao, *RSC Adv.* **2019**, *9*, 12615.

[9] D. S. Hyeon, G. Jang, S. Min, J. P. Hong, *Adv. Electron. Mater.* **2022**, *8*, 2100660.

[10] a) G. Bersuker, D. Gilmer, D. Veksler, P. Kirsch, L. Vandelli, A. Padovani, L. Larcher, K. McKenna, A. Shluger, V. Iglesias, *J. Appl. Phys.* **2011**, *110*, 124518; b) W. Lian, S. Long, H. Lü, Q. Liu, Y. Li, S. Zhang, Y. Wang, Z. Huo, Y. Dai, J. Chen, *Chin. Sci. Bull.* **2011**, *56*, 461.

[11] a) P. Cui, S. Seo, J. Lee, L. Wang, E. Lee, M. Min, H. Lee, *ACS Nano* **2011**, *5*, 6826; b) S. Lee, J. Sohn, Z. Jiang, H.-Y. Chen, H.-S. P. Wong, *Nat. Commun.* **2015**, *6*, 8407; c) Z. Shen, C. Zhao, Y. Qi, W. Xu, Y. Liu, I. Z. Mitrovic, L. Yang, C. Zhao, *Nanomaterials* **2020**, *10*, 1437; d) Z. Shen, C. Zhao, Y. Qi, I. Z. Mitrovic, L. Yang, J. Wen, Y. Huang, P. Li, C. Zhao, *Micromachines* **2020**, *11*, 341.

[12] a) T. Ninomiya, S. Muraoka, Z. Wei, R. Yasuhara, K. Katayama, T. Takagi, *IEEE Electron Device Lett.* **2013**, *34*, 762; b) H. Sun, H. Lv, Q. Liu, S. Long, M. Wang, H. Xie, X. Liu, X. Yang, J. Niu, M. Liu, *IEEE Electron Device Lett.* **2013**, *34*, 873.

[13] a) J. Díaz, G. Paolicelli, S. Ferrer, F. Comin, *Phys. Rev. B* **1996**, *54*, 8064; b) S. T. Jackson, R. G. Nuzzo, *Appl. Surf. Sci.* **1995**, *90*, 195; c) A. L. M. Reddy, A. Srivastava, S. R. Gowda, H. Gullapalli, M. Dubey, P. M. Ajayan, *ACS Nano* **2010**, *4*, 6337; d) X. Chen,

© 2023 The Authors. Advanced Electronic Materials published by Wiley-VCH GmbH

2199160x, 0, Downloaded from https://onlinelibrary.wiley.com/doi/10.1002/aelm.202201090 by Hanyang University Library, Wiley Online Library on [12/02/2023]. See the Terms and Conditions (https://onlinelibrary.wiley.com/terms-and-conditions) on Wiley Online Library for rules of use; OA articles are governed by the applicable Creative Commons License

X. Wang, D. Fang, *Fullerenes, Nanotubes, Carbon Nanostruct.* **2020**, *28*, 1048.

[14] a) P. Gielisse, *Diamond and Diamond-Like Film Applications*, CRC Press, Boca Raton, FL, USA **1998**; b) J. Vejpravová, *Nanomaterials* **2021**, *11*, 2469.

[15] a) N. P. Subramanian, X. Li, V. Nallathambi, S. P. Kumaraguru, H. Colon-Mercado, G. Wu, J.-W. Lee, B. N. Popov, *J. Power Sources* **2009**, *188*, 38; b) K. Stańczyk, R. Dziembaj, Z. Piwowarska, S. Witkowski, *Carbon* **1995**, *33*, 1383; c) M. K. Rabchinskii, S. D. Saveliev, D. Y. Stolyarova, M. Brzhezinskaya, D. A. Kirilenko, M. V. Baidakova, S. A. Ryzhkov, V. V. Shnitov, V. V. Sysoev, P. N. Brunkov, *Carbon* **2021**, *182*, 593.

[16] D. Marton, K. Boyd, A. Al-Bayati, S. Todorov, J. Rabalais, *Phys. Rev. Lett.* **1994**, *73*, 118.

[17] a) L. Lai, J. R. Potts, D. Zhan, L. Wang, C. K. Poh, C. Tang, H. Gong, Z. Shen, J. Lin, R. S. Ruoff, *Energy Environ. Sci.* **2012**, *5*, 7936; b) X. Duan, H. Sun, S. Wang, *Acc. Chem. Res.* **2018**, *51*, 678; c) S. Souto, M. Pickholz, M. Dos Santos, F. Alvarez, *Phys. Rev. B* **1998**, *57*, 2536.

[18] a) J. Robertson, C. Davis, *Diamond Relat. Mater.* **1995**, *4*, 441; b) Z. Luo, S. Lim, Z. Tian, J. Shang, L. Lai, B. MacDonald, C. Fu, Z. Shen, T. Yu, J. Lin, *J. Mater. Chem.* **2011**, *21*, 8038; c) J.-K. Chang, W.-H. Lin, J.-I. Taur, T.-H. Chen, G.-K. Liao, T.-W. Pi, M.-H. Chen, C.-I. Wu, *ACS Appl. Mater. Interfaces* **2015**, *7*, 17155.

[19] a) S. Chakrabarti, S. Samanta, S. Maikap, S. Z. Rahaman, H.-M. Cheng, *Nanoscale Res. Lett.* **2016**, *11*, 389; b) F.-C. Chiu, *Adv. Mater. Sci. Eng.* **2014**, 578168; c) K. González-Flores, P. Horley, S. Cabañas-Tay, S. Pérez-García, L. Licea-Jiménez, L. Palacios-Huerta, M. Aceves-Mijares, M. Moreno-Moreno, A. Morales-Sánchez, *Superlattices Microstruct.* **2020**, *137*, 106347; d) A. Zaman, G. Subramanyam, E. Shin, C. Yakopcic, T. M. Taha, A. E. Islam, S. Ganguli, D. Dorsey, A. Roy, *ECS J. Solid State Sci. Technol.* **2020**, *9*, 103003.

[20] a) J. A. Röhr, R. C. MacKenzie, *J. Appl. Phys.* **2020**, *128*, 165701; b) Z. Lü, Z. Deng, J. Zheng, Y. Zou, Z. Chen, D. Xu, Y. Wang, *Phys. E* **2009**, *41*, 1806; c) A. Rose, *Phys. Rev.* **1955**, *97*, 1538.

[21] a) D. Lehninger, R. Olivo, T. Ali, M. Lederer, T. Kämpfe, C. Mart, K. Biedermann, K. Kühnel, L. Roy, M. Kalkani, *Phys. Status Solidi A* **2020**, *217*, 1900840; b) H. Chen, L. Li, J. Wang, G. Zhao, Y. Li, J. Lan, B. K. Tay, G. Zhong, J. Li, M. Huang, *IEEE Electron Device Lett.* **2022**, *43*, 1141; c) S. Yu, P.-Y. Chen, *IEEE J. Solid-State Circuits* **2016**, *8*, 43.

[22] a) Z.-H. Sheng, L. Shao, J.-J. Chen, W.-J. Bao, F.-B. Wang, X.-H. Xia, *ACS Nano* **2011**, *5*, 4350; b) Y. L. Chueh, M. W. Lai, J. Q. Liang, L. J. Chou, Z. L. Wang, *Adv. Funct. Mater.* **2006**, *16*, 2243; c) Y. Baek, K. Yong, *J. Phys. Chem. C* **2007**, *111*, 1213.

[23] a) D. Geng, S. Yang, Y. Zhang, J. Yang, J. Liu, R. Li, T.-K. Sham, X. Sun, S. Ye, S. Knights, *Appl. Surf. Sci.* **2011**, *257*, 9193; b) S. Sandoval, N. Kumar, A. Sundaresan, C. Rao, A. Fuertes, G. Tobias, *Eur. J. Chem.* **2014**, *20*, 11999.

© 2023 The Authors. Advanced Electronic Materials published by Wiley-VCH GmbH

2199160x, 0, Downloaded from https://onlinelibrary.wiley.com/doi/10.1002/aelm.202201090 by Hanyang University Library, Wiley Online Library on [12/02/2023]. See the Terms and Conditions (https://onlinelibrary.wiley.com/terms-and-conditions) on Wiley Online Library for rules of use; OA articles are governed by the applicable Creative Commons License